



OPEN

SUBJECT AREAS:

BATTERIES

MATERIALS CHEMISTRY

NANOSCALE MATERIALS

Received

28 August 2013

Accepted

13 November 2013

Published

29 November 2013

Correspondence and
requests for materials
should be addressed to
S.Q.J. (sjiao@ustb.
edu.cn)

A new cathode material for super-valent battery based on aluminium ion intercalation and deintercalation

Wei Wang¹, Bo Jiang¹, Weiyi Xiong¹, He Sun¹, Zheshuai Lin², Liwen Hu¹, Jiguo Tu¹, Jungang Hou¹, Hongmin Zhu¹ & Shuqiang Jiao¹

¹State Key Laboratory of Advanced Metallurgy, University of Science and Technology Beijing, Beijing 100083, PR China,

²Technical Institute of Physics and Chemistry, Chinese Academy of Sciences, Beijing, 100190, P.R. China.

Due to their small footprint and flexible siting, rechargeable batteries are attractive for energy storage systems. A super-valent battery based on aluminium ion intercalation and deintercalation is proposed in this work with VO₂ as cathode and high-purity Al foil as anode. First-principles calculations are also employed to theoretically investigate the crystal structure change and the insertion-extraction mechanism of Al ions in the super-valent battery. Long cycle life, low cost and good capacity are achieved in this battery system. At the current density of 50 mA g⁻¹, the discharge capacity remains 116 mAh g⁻¹ after 100 cycles. Comparing to monovalent Li-ion battery, the super-valent battery has the potential to deliver more charges and gain higher specific capacity.

Renewable energy sources such as solar and wind have been widely used to generate electricity for green energy systems. These systems show huge potential for meeting the future energy demands^{1–3}. However, the electricity generated from these renewable sources are intermittent, and efficient electrical energy storage (EES) devices are needed for effective delivery of uninterrupted electricity (power storage back up) and load leveling as well as grid energy storage^{4,5}.

Nowadays, due to their outstanding energy and power density, Li-ion batteries have become a mainstay for EES^{6–9}. However, the concerns regarding the high cost and the limited lithium reserves in the earth's crust have driven the researchers to search more sustainable alternative energy storage solutions^{10–15}. Sodium-ion and magnesium-ion batteries, as new energy storage systems in portable devices, have attracted much attention of the investigators^{16–19}. Most recently, aluminium-ion battery with multivalent metal ions transmitting internally has been studied preliminarily^{20–23}. Owing to its low cost, easy operation and high security, the aluminium-ion battery has exhibited excellent prospects. However, the capacity and the cycle life are not satisfying at present. Some multivalent metal elements, such as aluminium and titanium, are abundant metallic elements in the earth's crust with low price. Most important of all, comparing to Li-ion and Na-ion batteries with only one charge transferred in one redox couple, batteries with multivalent metal ions running between anodes and cathodes can transfer more charges in one redox couple, indicating a promising energy storage device for large capacity. Herein, we define this kind of battery as super-valent battery.

Owing to its proper electrode potential and tunnel structure, VO₂ (B) with metastable monoclinic structure is generally used as a cathode material in Li-ion batteries. Li ions can freely insert and extract in these tunnels in reversible Li-ion batteries^{24–26}. In this work, VO₂ nanorods have been synthesized through a low temperature hydrothermal method. The super-valent battery based on aluminium ion intercalation and deintercalation has been assembled. The battery exhibits excellent reversibility, and long cycle life and high capacities have been acquired.

Results

Charge/discharge principle of the super-valent battery. The schematic representation of the super-valent battery based on aluminium ion during charge/discharge process is presented in Figure 1. In this example, Al foil serves as anode material and VO₂ pasted on stainless steel serves as cathode material.

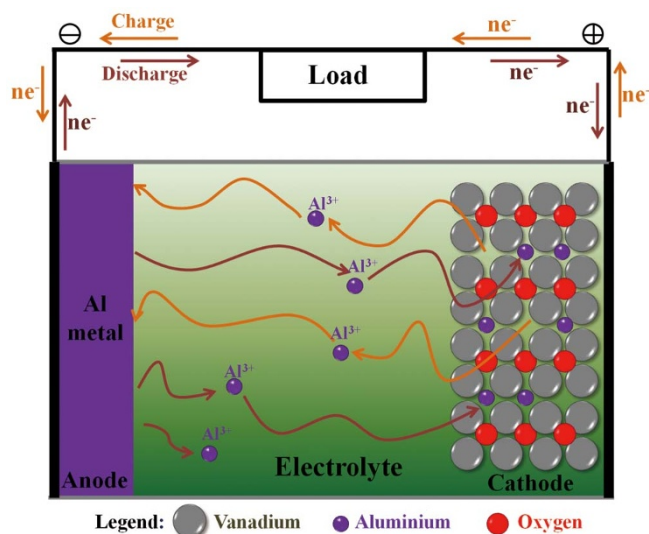
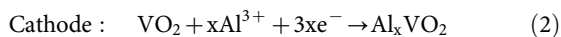
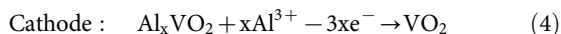
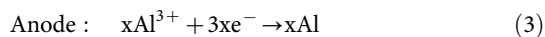


Figure 1 | Charge/discharge process. Schematic representation of the super-valent battery during charge/discharge process.

In the discharge process:



In the charge process:



Similar to “rocking-chair” Li-ion batteries, Al ions shuttle back and forth between the electrolyte and electrodes in this super-valent battery. When one Al ion moves from anode to cathode, three charges will transfer in the external circuits as compensation. Therefore, large capacity will be acquired in super-valent batteries, which ensures large-scale applications.

Computational simulations. In order to illustrate the insertion-extraction mechanism of Al ions in the VO_2 electrode, the first-principles plane-wave pseudopotential method²⁷ implemented in the CASTEP package²⁸ were employed to calculate the formation energy and unit cell volume change for Al-ion insertion. The parameters were set according to a modified method reported by Jiao’s group²⁹.

Generalized gradient approximation with norm-conserving pseudopotentials³⁰ was used with the plane-wave cut-off of 300 eV. In order to study Al insertion and extraction, it is necessary to consider a larger cell than the basic unit. Thus we construct a supercell of four primitive ($2 \times 2 \times 1$) cells consisting of 16 VO_2 molecules. Brillouine-zone integrations are made using ($2 \times 2 \times 4$) special- k -point meshes according to the Monkhorst-Pack scheme³¹. For each geometry optimization both atomic positions and lattice parameters are fully relaxed using the quasi-Newton method³². The convergence thresholds between optimization cycles for energy change, maximum force, maximum stress, and maximum displacement are set as 2×10^{-5} eV/atom, 0.05 eV/Å, 0.1 GPa, and 0.002 Å, respectively. The optimization terminates when all of these criteria are satisfied. The choice of these computational parameters ensures good convergence in present studies.

As shown in Figure 2a, there are four channels (V_4O_8) in our VO_2 structure. As Al ions are successively incorporated into one of the VO_2 channel (V_4O_8), the structure of the other three channels is slightly influenced. Herein, only one channel is taken into account to study the insertion of Al ions in this experiment. The formation energy is defined as:

$$E_f(\text{Al}) = E_{\text{tot}}[x\text{Al} + (\text{V}_4\text{O}_8)(\text{V}_{12}\text{O}_{24})]/16 - E_{\text{tot}}[(\text{V}_4\text{O}_8)(\text{V}_{12}\text{O}_{24})]/16 - x \cdot E_{\text{tot}}(\text{Al})/16 \quad (5)$$

Here $E_{\text{tot}}[x\text{Al} + (\text{V}_4\text{O}_8)(\text{V}_{12}\text{O}_{24})]$ is the total energy of the $[(\text{V}_4\text{O}_8)(\text{V}_{12}\text{O}_{24})]$ containing x Al atoms, $E_{\text{tot}}[(\text{V}_4\text{O}_8)(\text{V}_{12}\text{O}_{24})]$ is the total energy of the $[(\text{V}_4\text{O}_8)(\text{V}_{12}\text{O}_{24})]$ without any Al atom, and $E_{\text{tot}}(\text{Al})$ is the total energy of a Al atom in the reservoir (i.e., bulk Al).

The crystal structure of VO_2 is shown in Figure 2a, and the gray and red balls correspond to V and O atoms, respectively. The structure consists of sheets of edge sharing VO_6 octahedra linked by corner sharing to adjacent sheets along the c -direction of the unit cell³³.

Figure 2a to Figure 2e exhibit the relaxed atomic structures with different numbers of Al atoms in $[(\text{V}_4\text{O}_8)(\text{V}_{12}\text{O}_{24})]$. The structure of VO_2 (B) is built-up distorted VO_6 octahedra, sharing both corners and edges and forming the V-O tunnels. The Al atoms occupy the intervals of the V-O tunnels. The formation energy calculated by first-principles simulations with respect to the number of Al ions in a $[\text{Al}_x(\text{V}_4\text{O}_8)](\text{V}_{12}\text{O}_{24})$ is shown in Figure 2g. The more negative of the formation energy, the more stable are the Al ions located in the lattice. All formation energies are negative, demonstrating that these reactions can happen in theory.

As the number of Al atoms increases from 0 to 2, the changes of crystal structure are negligible and the VO_6 octahedra can be maintained. However, when it comes to $\text{Al}_3(\text{V}_4\text{O}_8)$ and $\text{Al}_4(\text{V}_4\text{O}_8)$, the VO_6 octahedra distorts badly. In this case, the bond length of V-O is ca. 3.6 Å and 3.7 Å, respectively, and actually the chemical bonds are deemed to be broken when the bond length is more than 3 Å. This can also be concluded from Figure 2h and Table 1. When 3 Al ions occupy the VO_2 channel (V_4O_8), the cell volume is enlarged about 16% compared to the initial cell. The longitudinal expansion of the V-O tunnel along the b and c axis is obvious while the a axis shrinks. The decrease of the a axis is mainly owing to the increased ionic bonding interactions between Al ions and $[\text{VO}_2]^{-1}$ as more Al ions insert into $[(\text{V}_4\text{O}_8)(\text{V}_{12}\text{O}_{24})]$. Another possible reason is that the Al ion screening effect is strengthened upon Al addition, leading to the decrease in the a axes³⁴. When $\text{Al}_3(\text{V}_4\text{O}_8)$ is formed, the length of the b and c axis suddenly increases to 10.73 Å and 5.75 Å, respectively, resulting in the breaking of the V-O chemical bonds.

Another situation of the insertion of Al atoms in $\text{V}_{16}\text{O}_{32}$ might be that, in the discharge process V atoms could be substituted by Al atoms. As shown in Figure 2f, one Al atom occupies the V atom site, forming $\text{AlV}_{15}\text{O}_{32}$. But the formation energy calculated by first-principles simulations is positive, that is:

$$\Delta E/E_v = 2.65 \text{ eV} > 0 \quad (6)$$

Therefore, this reaction cannot happen.

Characterization of the as-synthesized VO_2 . Figure 3a shows the X-ray diffraction pattern of the as-prepared powder along with standard pattern for VO_2 (JCPDS No. 81-2392)³⁵. All diffraction peaks of the as-prepared powder can be indexed to the monoclinic crystal structure of VO_2 (B) phase. The intensity and board width of the XRD peaks are a bit weak, which is primarily due to the tiny size of the phase, resulting in the smearing of the measured signal strength²⁹. The morphology and microstructure are gained by TEM and FESEM images displayed in Figure 3b and 3c. The as-prepared material has a rod-like morphology with sizes around

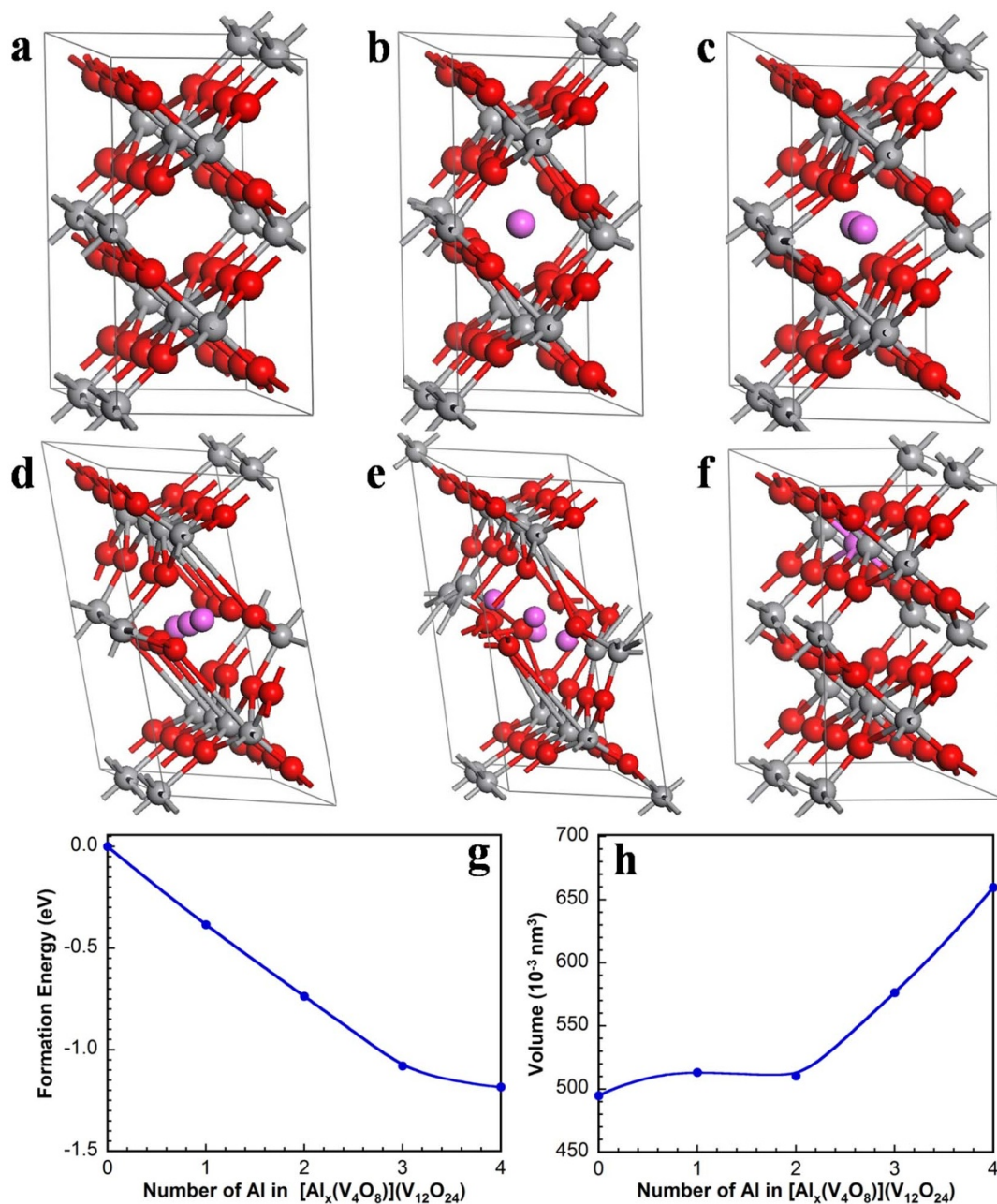


Figure 2 | First-principles calculations. (a–e) The atomic structures with 0, 1, 2, 3, 4 Al atoms in $[(V_4O_8)(V_{12}O_{24})]$. (f) The atomic structure of $AlV_{15}O_{32}$. The purple, red, and gray balls correspond to Al, O, and V atoms, respectively. (g) The relationship between the formation energy and the number of Al atoms in $[Al_x(V_4O_8)](V_{12}O_{24})$. The blue curve is the exponential fitting for the calculated results. (h) Volume with respect to the number of Al atoms in $[Al_x(V_4O_8)](V_{12}O_{24})$.

60–100 nm in width and about 1 μm in length. These nanorods tend to assemble to form bundles in the same direction. Figure 3c shows the FESEM image of the as-prepared VO_2 , from which it can be seen that a mass of rod-like VO_2 forms flower-like clusters.

Chemical formula	a(Å)	b(Å)	c(Å)	α	β	γ
$V_{16}O_{32}$	11.41	9.25	5.55	90.02	122.30	90.00
$[Al(V_4O_8)](V_{12}O_{24})$	11.16	9.74	5.50	88.68	120.72	90.08
$[Al_2(V_4O_8)](V_{12}O_{24})$	11.15	9.42	5.64	89.97	120.59	90.26
$[Al_3(V_4O_8)](V_{12}O_{24})$	10.80	10.73	5.75	79.03	117.50	89.55
$[Al_4(V_4O_8)](V_{12}O_{24})$	10.72	11.66	5.93	82.28	115.83	89.40

Specific surface area. The BET specific surface area is investigated by nitrogen adsorption–desorption isotherms, as is shown in Figure 4. The nitrogen-sorption measurements show a typical type IV isotherm, which implied the existence of mesopores. The BET specific surface area is as high as $37.3 \text{ m}^2\text{g}^{-1}$. The large surface area provides short diffusion lengths and the transport of Al ions and electrons in VO_2 is much easier.

Electrochemical performance. The cyclic voltammetry curves of the super-valent battery in the voltage window 0.01–0.9 V for the initial three cycles is shown in Figure 5a and a pair of redox peaks were observed clearly. The anodic and cathodic peaks were at 0.76 V and 0.47 V, respectively. The CV curves of the three cycles remained almost unchanged, demonstrating that the electrochemical reaction was stable and highly reversible.

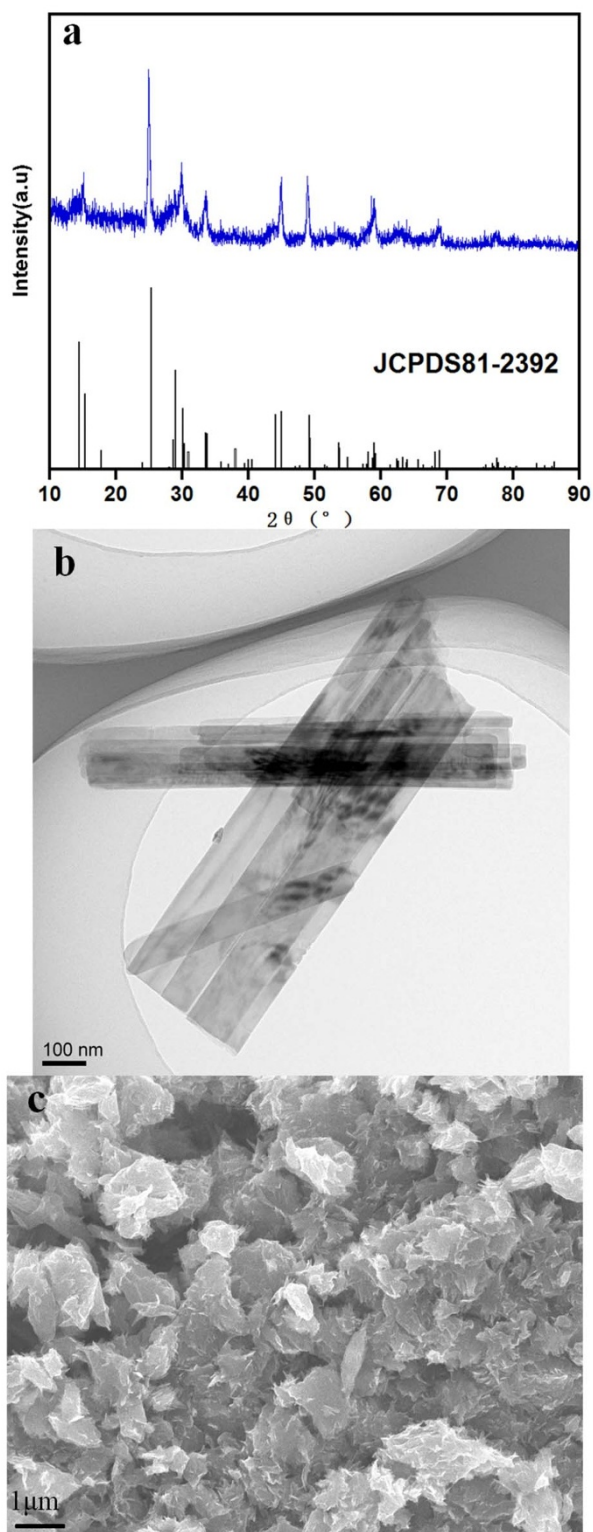


Figure 3 | Structure and morphology. (a) XRD patterns of VO₂ sample. TEM (b) and FESEM (c) images of VO₂ sample.

Figure 5b represents the initial three charge/discharge curves of VO₂ in an as-prepared cell at the current density of 50 mA g⁻¹. The cut-off voltage was set in the range of 0.01–0.9 V. Before the regular galvanostatic charge/discharge tests, the cells were cycled at a relatively low current density for over 10 h to fulfill the activation process. In the initial cycle, the as-prepared cell delivered a discharge capacity of 165 mA h g⁻¹. This might be explained by the following reaction:

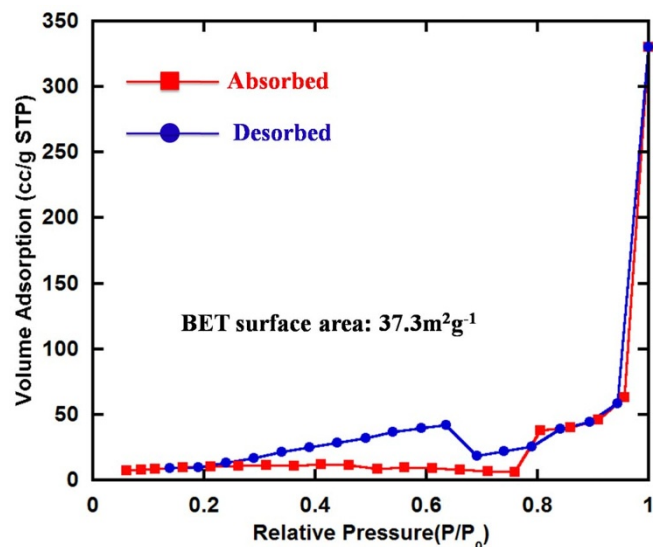
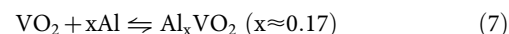


Figure 4 | Specific surface area. N₂ adsorption/desorption isotherm of as-synthesized VO₂ sample.



For all charge/discharge profiles, obvious charge and discharge voltage plateaus could be seen around 0.7 V and 0.5 V, respectively, which fitted well with the CV curves. The capacity loss of the initial three cycles was little, demonstrating a highly reversible reaction.

Cycling performances of VO₂ nanorods under different current densities are displayed in Figure 5c. At the current density of 50 mA g⁻¹, the discharge capacity remained 116 mA h g⁻¹ after 100 cycles. When it came to very high current densities of 100 mA g⁻¹ and 200 mA g⁻¹, the corresponding capacities could still retain 106 and 70 mA h g⁻¹, respectively. We could conclude that, in this voltage range, the crystalline structure of the as-prepared powder could shuttle Al ions back and forth and remained stable. It is worth mentioning that if two Al ions could insert into V₄O₈ (Figure 2c), the theoretical capacity could reach to as high as 485 mA h g⁻¹. Therefore, there is still a great space for improvement of capacity.

XPS spectrum. XPS measurement is carried out to analyze the valent state of vanadium after a discharge process, as is shown in Figure 6. After discharging at a low current density of 20 mA g⁻¹, both V³⁺ and V⁴⁺ appear, which agrees with reaction (7).

Discussion

A super-valent battery based on aluminium ion intercalation and deintercalation has been proposed and its electrochemical performance has been demonstrated. The cell can provide a discharge capacity of 165 mA h g⁻¹ in the initial cycle and retain 116 mA h g⁻¹ after 100 cycles. High current density capabilities and long-term performance have been achieved in this work. All results represent a new strategy for the development of inexpensive and stable energy storage. Some new battery systems such as aqueous rechargeable lithium batteries have been reported recently³⁶ and their energy densities range from 40–90 Wh kg⁻¹. Comparing with these battery systems, the energy density of this system is a bit low (48 Wh kg⁻¹ at 50 mA g⁻¹), but it is worth trying. The researches about the super-valent battery will continue for its low cost and bright prospect.

Due to the variable valence and relative stability at different valence state of transition metal, the transition metal oxides and transition metal salts should be given priority attention to develop new kind of cathode materials. In order to let Al³⁺ ions shuttle back and forth in

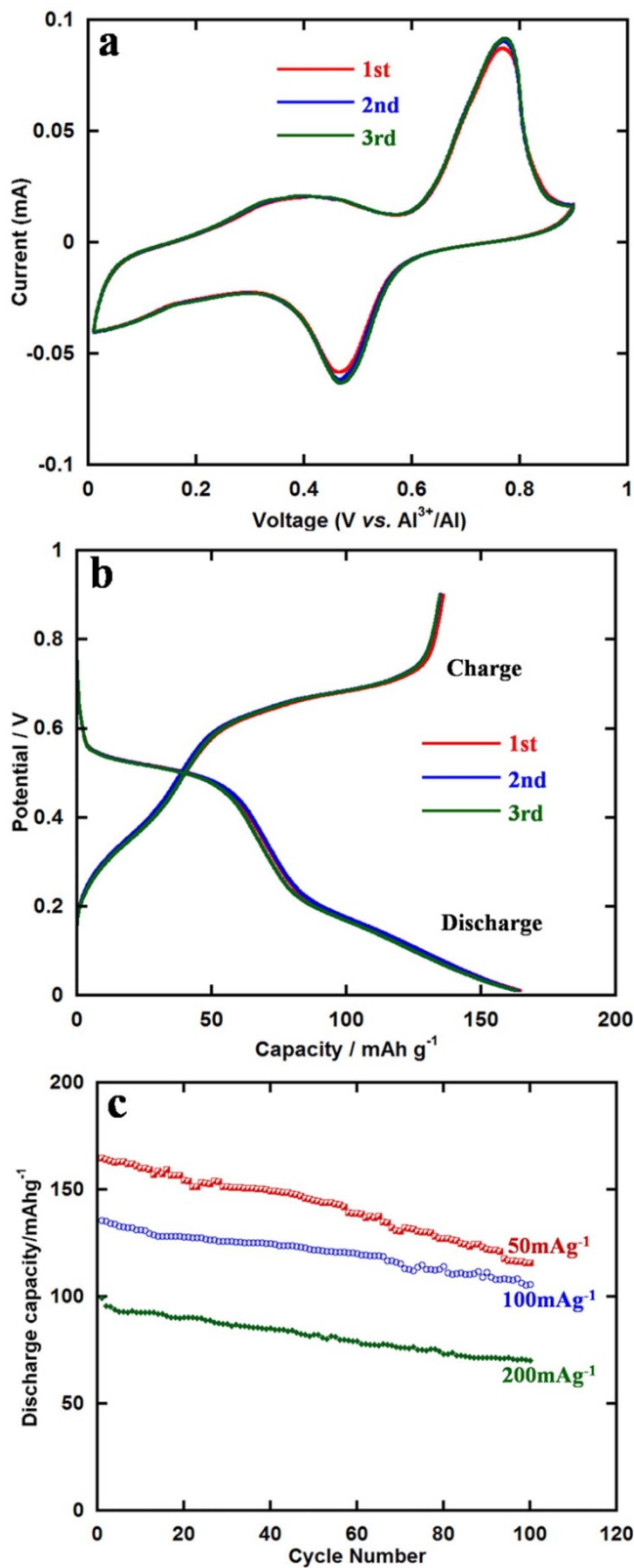


Figure 5 | Electrochemical performance. (a) Cyclic voltammograms curves of VO_2 at the scan rate of 0.1 mVs^{-1} in the voltage range of $0.01\text{--}0.9 \text{ V}$. (b) The initial three charge/discharge curves at the current density of 50 mA g^{-1} . (c) Cycling performances under different current densities over 100 cycles.

the electrode materials in this super-valent battery, materials with large channel or layered structure should also be the our first priority.

It is the first time that super-valent battery based on aluminium ion could maintain a capacity at this level for 100 cycles. Although the

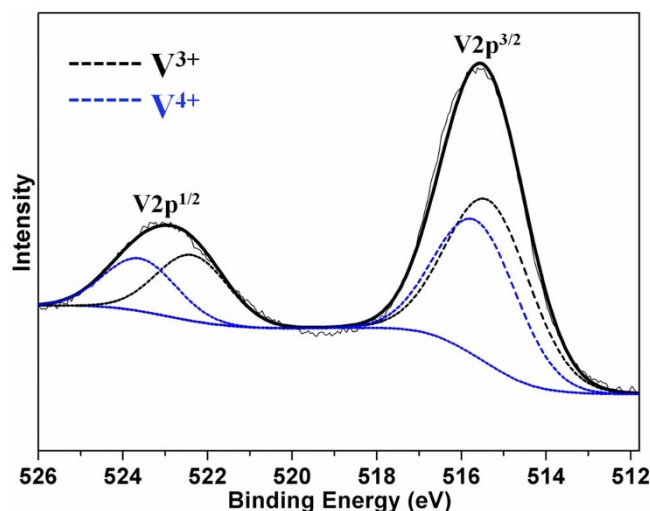


Figure 6 | XPS spectra. XPS V 2p spectra of as-prepared VO_2 after a discharge process.

voltage plateau was a bit low and the capacity was not that high, the attempt to develop super-valent battery was worth pondering. More researches need to be done in the future to further analyze the storage mechanism of metal ions and commercialize the super-valent batteries, including the exploration of cathode materials with higher cell voltages and specific capacities, electrolyte optimization and seeking other multivalent metal ions for super-valent batteries.

Methods

Synthesis. In a typical preparing process, 0.7275 g (4 mmol) V_2O_5 and 1.5128 g (12 mmol) $\text{H}_2\text{C}_2\text{O}_4 \cdot 2\text{H}_2\text{O}$ were dissolved in a 20 mL of deionized water under continuously stirring at 80°C for 1 h and a blue clear solution was formed. And then the solution was cooled down to room temperature. $\text{NH}_3 \cdot \text{H}_2\text{O}$ solution ($28 \text{ wt}\%$ NH_3) was applied as pH adjustment agent in this experiments, and it was dropped into the blue solution until the pH value was adjusted to 9.0 . The newly formed suspension was washed by deionized water and alcohol for several times and dried at 80°C overnight. The as-prepared powder was grinded in an agate mortar for 30 minutes and then 0.1 g was dissolved into a 20 mL of 0.1 g/mL PEG-600 solution under continuously stirring for 1 h . Then the solution was transferred into a 25 mL Teflon-lined autoclave with stainless steel shell for hydrothermal reaction at 200°C for 24 h . The precipitate was collected with distilled water and alcohol by a centrifuger and then dried in an oven at 120°C for 12 h .

Characterization. The crystal structure of the samples was determined by an X-ray diffractometer (XRD, Rigaku, D/max-RB). The morphology was characterized by transmission electron microscopy (TEM, JEOL, JEM-2010) and field emission scanning electron microscope (FESEM, JEOL, JSM-6701F). The surface area measurements were performed according to the Brunauer-Emmett-Teller (BET) method.

Cell Fabrication and electrochemical measurements. Electrochemical measurements were performed with 2032 coin cells with high-purity Al foil as counter and reference electrodes. The working electrode was prepared by mixing active materials, acetylene black and teflon (poly(tetrafluoroethylene), PTFE) binder at a weight ratio of $75:15:10$. The resultant slurry was then coated uniformly on stainless steel and dried at 120°C for 12 h . The electrolyte was prepared by mixing AlCl_3 and 1-butyl-3-methylimidazolium chloride together with $1:1$ molar ratio to form the ionic liquid. Approximately $0.5 \text{ wt}\%$ benzyl sulfoxide ($\text{C}_{14}\text{H}_{14}\text{OS}$) to the above-mentioned electrolyte was used as corrosion inhibitor. A glass fiber (GF/D) from Whatman was used as the separator. The coin cells were assembled in an argon-filled glove box and galvanostatically cycled at different current densities in the voltage range of $0.01\text{--}0.9 \text{ V}$ using NEWARE battery testing system. The specific capacity and current density were calculated based on the mass of active material.

- Linic, S., Christopher, P. & Ingram, D. B. Plasmonic-metal nanostructures for efficient conversion of solar to chemical energy. *Nat. Mater.* **10**, 911–921 (2011).
- Zhou, Y., Luckow, P., Smith, S. J. & Clarke, L. Evaluation of global onshore wind energy potential and generation costs. *Environ. Sci. Technol.* **46**, 7857–7864 (2012).
- Kaltenbrunner, M. *et al.* Ultrathin and lightweight organic solar cells with high flexibility. *Nat. Commun.* **3**, 770 (2012).



4. Dennler, G., Scharber, M. C. & Brabec, C. J. Polymer-fullerene bulk-heterojunction solar cells. *Adv. Mater.* **21**, 1323–1338 (2009).
5. Ackermann, T. & Soder, L. An overview of wind-energy status 2002. *Renew. Sust. Energ. Rev.* **6**, 67–128 (2002).
6. Tarascon, J. M. & Armand, M. Issues and challenges facing rechargeable lithium batteries. *Nature* **414**, 359–367 (2001).
7. Kang, K., Meng, Y. S., Br egger, J., Grey, C. P. & Ceder, G. Electrodes with high power and high capacity for rechargeable lithium batteries. *Science* **311**, 977–980 (2006).
8. Ge, M., Rong, J., Fang, X. & Zhou, C. Porous Doped silicon nanowires for lithium ion battery anode with long cycle life. *Nano Lett.* **12**, 2318–2323 (2012).
9. Tepavcevic, S. *et al.* Nanostructured bilayered vanadium oxide electrodes for rechargeable sodium-ion batteries. *ACS nano* **6**, 530–538 (2012).
10. Li, C., Ji, W., Chen, J. & Tao, Z. Metallic aluminum nanorods: synthesis via vapor-deposition and applications in Al/air batteries. *Chem. Mater.* **19**, 5812–5814 (2007).
11. Hueso, K. B., Armand, M. & Rojo, T. High temperature sodium batteries: status, challenges and future trends. *Energy Environ. Sci.* **6**, 734–749 (2003).
12. Li, Y. *et al.* Advanced zinc-air batteries based on high-performance hybrid electrocatalysts. *Nat. Commun.* **4**, 1805 (2013).
13. Licht, S., Wang, B. & Ghosh, S. Energetic iron(VI) chemistry: The super-iron battery. *Science* **285**, 1039–1042 (1999).
14. Cheng, F., Liang, J., Tao, Z. & Chen, J. Functional materials for rechargeable batteries. *Adv. Mater.* **23**, 1695–1715 (2011).
15. Lee, J. S. *et al.* Metal–air batteries with high energy density: Li–air versus Zn–air. *Adv. Energy Mater.* **1**, 34–50 (2011).
16. Ellis, B. L. & Nazar, L. F. Sodium and sodium-ion energy storage batteries. *Curr. Opin. Solid St. M.* **16**, 168–177 (2012).
17. Slater, M. D., Kim, D., Lee, E. & Johnson, C. S. Sodium-ion batteries. *Adv. Funct. Mater.* **23**, 947–958 (2013).
18. Pour, N., Gofer, Y., Major, D. T. & Aurbach, D. Structural analysis of electrolyte solutions for rechargeable Mg batteries by stereoscopic means and DFT calculations. *J. Am. Chem. Soc.* **133**, 6270–6278 (2011).
19. Feng, Z., Yang, J., NuLi, Y. & Wang, J. Sol-gel synthesis of Mg_{1.03}Mn_{0.97}SiO₄ and its electrochemical intercalation behavior. *J. Power Sources* **184**, 604–609 (2008).
20. Jayaprakash, N., Das, S. K. & Archer, L. A. The rechargeable aluminum-ion battery. *Chem. Commun.* **47**, 12610–12612 (2011).
21. Liu, S. *et al.* Aluminum storage behavior of anatase TiO₂ nanotube arrays in aqueous solution for aluminum ion batteries. *Energy Environ. Sci.* **5**, 9743–9746 (2012).
22. Rani, J. V., Kanakaiah, V., Dadmal, T., Rao, M. S. & Bhavanarushi, S. Fluorinated natural graphite cathode for rechargeable ionic liquid based aluminum–ion battery. *J. Electrochem. Soc.* **160**, A1781–A1784 (2013).
23. Reed, L. D. & Menke, E. The roles of V₂O₅ and stainless steel in rechargeable Al–ion batteries. *J. Electrochem. Soc.* **160**, A915–A917 (2013).
24. Murphy, D. W., Christian, P. A., Disalvo, F. J., Carides, J. N. & Waszczak, J. V. Lithium incorporation by V₆O₁₃ and related vanadium (+4, +5) oxide cathode materials. *J. Electrochem. Soc.* **128**, 2053–2060 (1981).
25. Nethravathi, C., Viswanath, B., Michael, J. & Rajamath, M. Hydrothermal synthesis of a monoclinic VO₂ nanotube–graphene hybrid for use as cathode material in lithium ion batteries. *Carbon* **50**, 4839–4846 (2012).
26. Nethravathi, C. *et al.* N-doped graphene–VO₂(B) nanosheet-built 3D flower hybrid for lithium ion battery. *ACS Appl. Mater. Inter.* **5**, 2708–2714 (2013).
27. Payne, M. C., Teter, M. P., Allan, D. C., Arias, T. A. & Joannopoulos, J. D. Iterative minimization techniques for ab initio total-energy calculations: molecular dynamics and conjugate gradients. *Rev. Mod. Phys.* **64**, 1045–1097 (1992).
28. Clark, S. J. *et al.* First principles methods using CASTEP. *Z. Kristallogr.* **220**, 567–570 (2005).
29. Wang, W. *et al.* Microspheric Na₂Ti₃O₇ consisting of tiny nanotubes: an anode material for sodium-ion batteries with ultrafast charge–discharge rates. *Nanoscale* **5**, 594–599 (2013).
30. Lin, J. S., Qtseish, A., Payne, M. C. & Heine, V. Optimized and transferable nonlocal separable ab initio pseudopotentials. *Phys. Rev. B* **47**, 4174–4180 (1993).
31. Monkhorst, H. J. & Pack, J. D. On special points for brillouin zone integrations. *Phys. Rev. B* **13**, 5188–5192 (1976).
32. Fischer, T. H. & Almlof, J. General Methods for Geometry and Wave Function Optimization. *J. Phys. Chem.* **96**, 9768–9774 (1992).
33. Th ebald, F., Cabala, R. & Bernard, J. Essai sur la structure de VO₂(B). *J. Solid State Chem.* **17**, 431–438 (1976).
34. Hamani, D., Ati, M., Tarascon, J. M. & Rozier, P. Na_xVO₂ as possible electrode for Na-ion batteries. *Electrochem. Commun.* **13**, 938–941 (2011).
35. Oka, Y., Yao, T., Yamamoto, N., Ueda, Y. & Hayashi, A. Phase transition and V⁴⁺–V⁵⁺ pairing in VO₂(B). *J. Solid State Chem.* **105**, 271–278 (1993).
36. Tang, W. *et al.* Aqueous rechargeable lithium batteries as an energy storage system of superfast charging. *Energy Environ. Sci.* **6**, 2093–2104 (2012).

Acknowledgments

The work was supported by the National Natural Science Foundation of China (No.51322402), the Program for New Century Excellent Talents in University, Ministry of Education of China (NCET-2011-0577), and the Fundamental Research Funds for the Central Universities (FRF-TP-12-002B).

Author contributions

S.J. conceived the project. S.J. and W.W. designed and carried out the experiments, analyzed data and wrote the paper. B.J. and Z.L. carried out the computational study. W.W., W.X. and H.S. conducted XRD experiments. W.W., L.H. and J.T. did the TEM. J.H. and H.Z. provided scientific advice. All authors reviewed the manuscript.

Additional information

Competing financial interests: The authors declare no competing financial interests.

How to cite this article: Wang, W. *et al.* A new cathode material for super-valent battery based on aluminium ion intercalation and deintercalation. *Sci. Rep.* **3**, 3383; DOI:10.1038/srep03383 (2013).



This work is licensed under a Creative Commons Attribution-NonCommercial-NoDerivs 3.0 Unported license. To view a copy of this license, visit <http://creativecommons.org/licenses/by-nc-nd/3.0>